PARAMETERIZATIONS OF DEPOSITIONAL GROWTH OF CLOUD ICE IN A BULK MICROPHYSICAL SCHEME

Scott A. Braun, Brad S. Ferrier, and Wei-Kuo Tao

Summary

The Goddard Cumulus Ensemble model and other models use a technique for simulating clouds that includes three types of ice particles: very small cloud ice, larger snow crystals, and more dense graupel or hail. The cloud ice particles are important because they produce the large ice clouds that are blown off by thunderstorms at high levels in the atmosphere. These cloud ice particles grow by the transfer of water vapor onto the particles when the relative humidity is very high. As the ice particles grow larger, they eventually become snow. In previous versions of the cloud model, this growth process was incorrect because it did not depend on the relative humidity of the air. Two corrections for this process are presented that provide the needed relative humidity dependence. Computer simulations of thunderstorm lines shows a large impact of the corrections.

Another aspect of the cloud model that is examined is an adjustment that changes excess water vapor (i.e., that portion above the amount that the air can hold) into cloud water or cloud ice. When the excess water vapor is allowed to form cloud ice, the model produces possible errors in the growth of cloud water, ice and snow. It is shown that a significant portion of the cloud ice produced by the model within strongly rising air in thunderstorms is the result of this adjustment rather than from more realistic cloud processes.

PARAMETERIZATIONS OF DEPOSITIONAL GROWTH OF CLOUD ICE IN A BULK MICROPHYSICAL SCHEME

Scott A. Braun

Laboratory for Atmospheres, NASA/Goddard Space Flight Center, Greenbelt, Maryland

Brad S. Ferrier

Joint Center for Earth Systems Technology, University of Maryland, Baltimore County, Catonsville, Maryland

Wei-Kuo Tao

Laboratory for Atmospheres, NASA/Goddard Space Flight Center, Greenbelt, Maryland

Submitted to the

Journal of the Atmospheric Sciences

September 1, 1999

Corresponding Author: Dr. Scott A. Braun, Mesoscale Atmospheric Processes Branch, NASA/GSFC, Code 912, Greenbelt, MD 20771. braun@gilbert.gsfc.nasa.gov.

ABSTRACT

Two aspects of the cloud ice parameterization in the Goddard Cumulus Ensemble Model cloud physics parameterization are examined: the conversion of cloud ice to snow by depositional growth, designated PSFI, and the saturation adjustment scheme. The original formulation of PSFI is shown to produce excessive conversion of cloud ice to snow because of an implicit assumption that the relative humidity is 100% with respect to water even though the air may actually be quite less humid. Two possible corrections to this problem are proposed, the first involving application of a relative humidity dependent correction factor to the original formulation of PSFI, and the second involving a new formulation of PSFI based on the equation for depositional growth of cloud ice. The sensitivity of these formulations of PSFI to the assumed masses of the ice particles is examined. Possible problems associated with using a saturation adjustment scheme for cloud ice are discussed and simulations of a squall line with and without application of the adjustment scheme for ice are compared.

1. Introduction

The Goddard Cumulus Ensemble model (GCE, Tao and Simpson 1993; Tao and Soong 1986; Tao et al. 1993, 1996) cloud microphysics scheme is patterned after the schemes of Hsie et al. (1980; hereafter HFO) and Lin et al. (1983; hereafter LFO), but includes some modifications for cloud ice based upon the parameterizations of Rutledge and Hobbs (1983; hereafter RH). The parameterization includes three phases of ice: small cloud ice particles, larger snow crystals, and more dense graupel or hail particles. The cloud ice particles are important because they contribute significantly to the depth, width, and optical thickness of the anvil clouds generated by convection, which can significantly impact the transfer of solar and terrestrial radiation in the troposphere. Important process in the budget for cloud ice are the initiation of new cloud ice and the conversion of cloud ice to snow as the ice crystals grow to the size of snow particles by deposition. Examination of some components of the microphysics scheme reveals some potential problems or inconsistencies in the parameterization of the cloud ice processes. In this study, we discuss these problems and suggest some solutions.

One of the problems in the LFO and GCE ice schemes is the parameterization of the conversion of cloud ice to snow as ice grows by vapor deposition in the presence of cloud water, usually referred to as the Bergeron process and designated PSFI. Krueger et al. (1995) pointed out that PSFI converts ice to snow even when there is no cloud water. In fact, it converts ice to snow independent of the supersaturation with respect to ice and, as a result, produces excessive conversion of ice to snow. Since the cloud ice is assumed not to fall while snow does fall, Krueger et al. suggested that the excessive conversion of ice to snow via PSFI acts as a crude parameterization of cloud ice fallout. This note describes an alternative formulation of PSFI, based on the equation for depositional growth in RH, that is dependent on the supersaturation with respect to ice.

A second potential problem is related to the saturation adjustment scheme (Tao et al. 1989), which removes supersaturations with respect to water or ice (or both) depending on the temperature and on the relative amounts of cloud water and ice. Use of such a saturation adjustment scheme can produce cloud water at relative humidities less than saturation and lead to possible errors in the growth rates of ice and snow. We will compare simulations with and without the saturation adjustment scheme to check for physical consistency of the results.

2. Numerical Model

The discussion will be supported with numerical simulations of the 10-11 June 1985 PRE-STORM[1] squall line (Johnson and Hamilton 1988; Rutledge et al. 1988; Tao et al. 1993) using the two-dimensional version of the GCE model. The model equations are anelastic and the cloud microphysics include a parameterized Kessler-type two category liquid, three-category ice (cloud ice, snow, graupel/hail) scheme following LFO and Rutledge and Hobbs (1983, 1984). Further details about the model can be found in Tao et al. (1993, 1996).

A stretched vertical grid with 33 grid points and grid spacings from 150 m at low levels to 1000 m near model top (19 km) was used in order to maximize resolution in the lowest levels of the model. The horizontal grid consisted of 1026 grid points, the central 871 of which comprised the fine-grid area with a constant 1-km resolution. Outside of this region, the grid spacing was horizontally stretched with a ratio of 1.05:1 between adjacent grid points. Open lateral boundary conditions were used (Klemp and Wilhelmson 1978). A 5-km deep Rayleigh relaxation (absorbing) layer was used at the top of the model. Forward time differencing and a positive-definite advection scheme with a nonoscillatory option (Smolarkiewicz and Grabowski 1990) are used for all scalar variables (potential temperature, vapor mixing ratio, and all hydrometeor categories). A fourth-order accurate advection scheme and leapfrog time integration are used for the velocity components. The calculations used a time step of 6 s.

The model basic state is derived from the 2330 UTC 11 June 1985 sounding taken at Pratt, Kansas. This sounding is characterized by convective available potential energy of 2300 J kg^{-1}. The wind profile has been modified at upper levels to reduce the shear magnitude (see Tao et al. 1993). Convection is initiated by applying a cooling rate of up to 36 K h^{-1} over an area 65 km wide and 2.4 km deep for the first 600 s of the simulation.

Along with changes to the ice microphysical code related to PSFI and the saturation adjustment scheme, a few other minor modifications (summarized in Appendix A) have been made that generally produce only minor changes in the results. Table 1 summarizes the simulations included in this study. Each case is designated by the particular formulation of PSFI (of which there are three), the cloud-ice masses used in the parameterization (either values from HFO or from RH), and, in some cases, by other letters. The three formulations of PSFI and the definitions and values of the ice masses are provided in the next section. For consistency with the equations in Koenig (1971) and LFO and the coding of the numerical model, all equations and variables are written in cgs units.

3. Problems in the cloud ice parameterization

a. Conversion of cloud ice to snow

The basis for the parameterization of the Bergeron growth process in the ice microphysics scheme is Koenig's (1971) equation for the depositional growth of ice crystals at 100% relative humidity with respect to water,

$$\frac{dm}{dt} = a_1 m^{a_2}, \tag{1}$$

[1] Preliminary Region Experiment for the Stormscale Operational and Research Meteorology Program (Cunning 1986).

where m is the crystal mass in grams and a_1 and a_2 are temperature dependent parameters [see Table 4 of Koenig (1971)]. HFO and LFO expressed the conversion of cloud ice to snow through vapor deposition as

$$\mathrm{PSFI} = \frac{q_i}{\Delta t_1}, \tag{2}$$

where Δt_1 is the time required for an ice particle to grow from some initial size m_0 to some specified size considered representative of a small snow particle, m_s. According to (1), Δt_1 can be written as

$$\Delta t_1 = \int_{m_0}^{m_s} \frac{1}{a_1} \frac{dm}{m^{a_2}} = \frac{1}{a_1(1-a_2)}\left[m_s^{(1-a_2)} - m_0^{(1-a_2)}\right] \tag{3}$$

and PSFI can be written as

$$\mathrm{PSFI}_1 = \frac{a_1(1-a_2)q_i}{\left[m_s^{(1-a_2)} - m_0^{(1-a_2)}\right]}. \tag{4}$$

We will refer to (4) as the "original HFO" formulation of PSFI and designate it with the subscript 1.

Following from Koenig's (1971) formulation for a_1 and a_2, PSFI_1 depends only on temperature and the specified ice crystal masses m_0 and m_s, values for which can be obtained from HFO or from other mass-diameter relationships. As currently coded in the models, PSFI_1 is independent of the supersaturation with respect to ice (i.e., 100% relative humidity with respect to water is implicit) and overestimates the conversion rate for regions with relative humidities

less than 100% with respect to water. Furthermore, $PSFI_1$ can be active even when the relative humidity is less than or equal to the ice saturation value.

A simple correction to the original HFO formulation of PSFI is obtained by multiplying (4) by an empirically derived relative humidity factor (Hindman and Johnson 1972; Reisner et al. 1998)

$$\mathrm{PSFI}_2 = \frac{(q_v - q_{si})}{(q_{sw} - q_{si})} \frac{a_1(1-a_2)q_i}{\left[m_s^{(1-a_2)} - m_0^{(1-a_2)}\right]}, \quad q_v > q_{si} \tag{5}$$

where q_v, q_{si}, and q_{sw} are the vapor mixing ratio, and the saturation vapor mixing ratios over ice and water, respectively. Equation (5), which will be referred to as the "modified HFO" formulation of PSFI and designated $PSFI_2$, allows $PSFI_2$ to be equivalent to Eq. (4) when the relative humidity is 100% and to decrease to zero as q_v approaches the ice saturation value.

Another alternative formulation of PSFI can be derived from the ice depositional growth rate equation of RH,

$$\frac{dm}{dt} = \frac{4\overline{D}_i(S_i - 1)}{A'' + B''} \tag{6}$$

where $\overline{D}_i$ is the mean diameter of the ice crystals, $S_i = q_v/q_{si}$ is the supersaturation with respect to ice, and A'' and B'' are essentially temperature dependent parameters given below (A16) in RH. RH assumed hexagonal plate-like crystals and used the mass-diameter relationship $\overline{D}_i = 51.5m^{1/2}$, where m is the average crystal mass in grams and $\overline{D}_i$ is the crystal diameter in centimeters. Substituting m for $\overline{D}_i$ in (6) gives

$$\frac{dm}{dt} = \frac{206.2(S_i - 1)m^{1/2}}{(A'' + B'')}. \tag{7}$$

Equation (7) can be expressed in a form similar to (1) by setting $a_1 = 206.2(S_i - 1)/(A'' + B'')$ and $a_2 = 0.5$. Equation (4) then gives

$$\mathrm{PSFI}_3 = \frac{0.5 a_1 q_i}{\left[m_s^{1/2} - m_0^{1/2}\right]}. \tag{8}$$

Equation (8) will be referred to as the RH formulation of PSFI and will be designated PSFI_3. In this formulation, a_1 is both temperature and relative humidity dependent and approaches zero as the vapor mixing ratio approaches the ice saturation value. Unlike (4)-(5), PSFI_3 is consistent with the cloud ice depositional growth rate (6) used in the model. The values of a_1 in (8) can be compared to the values from Koenig (1971) if we consider relative humidities with respect to water of 100% (Figure 1). Koenig's values reach a maximum value near 258 K and show large variations with temperature because of assumptions of different particle habits for different temperature regimes. The values of a_1 from PSFI_3 are also maximum near 258 K, but show a smoother and much smaller variation with temperature because of the assumption of a single particle habit.

Ice crystal masses from the RH formulation can be substantially different from the masses used by HFO for the same assumed size. HFO set m_0 and m_s to the masses corresponding to 40 micron (m_0=2.46×10^{-7} g) and 50 micron (m_s=4.80×10^{-7} g) radius ice crystals. Krueger et al. (1995) suggested that 100 microns was a more realistic radius for small snow crystals, which gives m_s=3.84×10^{-6} g. If we use the mass-diameter relationship of RH,

then m_0=2.41×10^{-8} g for a 40 micron radius particle, m_s=3.76×10^{-8} g for a 50 micron particle, and m_s=1.51×10^{-7} g for a 100 micron particle, all of which are about an order of magnitude smaller than the values from HFO. The sensitivity of the numerical results to the varying estimates of m_0 and m_s will be examined later. The designation of HFO or RH in the case name indicates which mass values are used in that case.

Figure 2 shows magnitudes of PSFI based on the three formulations above: the original HFO formulation, $PSFI_1$ (4), the modified HFO formulation, $PSFI_2$ (5), and the RH formulation, $PSFI_3$ (8). The calculations assume m_0 and m_s corresponding to the masses of 40 and 100-micron radius particles using the RH mass-diameter relationship. The cloud ice mixing ratio is calculated assuming 40-micron sized particles in concentrations that vary with temperature following Fletcher (1962) (Eq. A2), $q_i = m_0 n_c / \rho$, where ρ is the air density. Figure 2a clearly shows the temperature dependence of the original HFO formulation and the lack of dependence upon relative humidity. The rates remain the same even when the air is subsaturated with respect to ice. The rates increase with decreasing temperature (increasing height) as a result of the increasing number concentration of cloud ice specified by the Fletcher equation. Figure 3 shows the snow and cloud ice distributions for case $PSFI_1$RH averaged over hours 5-6 of the simulation (using output saved every 10 min). The snow field (Fig. 3a) shows an anvil slightly wider than 150 km, with large mixing ratios contained in the leading convective cells and smaller, more horizontally uniform values in the trailing stratiform region. The cloud ice distribution (Fig. 3b) is similarly characterized by large values within convective cells, but values in the trailing stratiform

region are quite small, a result that will be shown to be caused by excessive conversion of cloud ice to snow by $PSFI_1$.

When the empirically derived relative humidity correction is applied (Fig. 2b, $PSFI_2$), the conversion rates for a given temperature are forced to decrease from a maximum value at 100% relative humidity with respect to water to zero at the ice saturation value. The RH formulation (Fig. 2c, $PSFI_3$) produces a qualitatively similar distribution to the modified HFO formulation, but the magnitudes are larger because, at these colder temperatures, the parameter a_1 for $PSFI_3$ is larger than the Koenig value. Figure 2d shows the difference between the RH formulation and the original HFO formulation ($PSFI_1$-$PSFI_3$). For ice supersaturations exceeding 10%, the RH formulation produces larger growth rates while for small ice supersaturations (<10%) and subsaturated conditions, the original HFO formulation produces larger growth rates, particularly at colder temperatures.

The above results imply that $PSFI_1$ will cause excessive transfer of ice to snow in the upper portion of clouds that exist in conditions of near saturation with respect to ice. This fact is demonstrated clearly with the numerical results shown in Fig. 4, which depict the snow and cloud ice fields for $PSFI_3$ (case $PSFI_3RH$). The snow field (Fig. 4a) shows somewhat reduced mixing ratios in the convective region compared to the case using $PSFI_1$ (Fig. 3a) while the cloud ice field (Fig. 4b) shows substantially greater mixing ratios within most of the anvil, including the trailing stratiform region. In particular, $PSFI_3$ leads to a broadening of the anvil cloud and an increase in cloud-top height of about 2-4 km. As in case $PSFI_1RH$, case $PSFI_3RH$ results in relative humidities near the ice saturation value (Fig. 10b) above ~8.5 km. In case $PSFI_1RH$, cloud ice was transferred to snow even though depositional growth was negligible, while in case $PSFI_3RH$, no

transfer of ice to snow occurred so that cloud ice accumulated in the anvil. If the accumulation of ice in the anvil becomes excessive (as determined by either objective or subjective measures), then the accumulation of cloud ice can be controlled explicitly through inclusion of cloud ice fallout as opposed to having PSFI cause excessive transfer of ice to snow and subsequent fallout of the snow.

To further demonstrate the sensitivity of the cloud ice fields to each formulation of PSFI and to the particle masses m_0 and m_s, Fig. 5 shows contoured frequency by altitude diagrams (CFADs, Yuter and Houze 1995) for cloud ice. The CFAD is a statistical analysis approach developed by Yuter and Houze (1995) that succinctly summarizes the frequency distribution of a variable in a given volume in a single contour plot. The ordinate of the plot is height, the abscissa is the value of the parameter whose distribution is being plotted, and the contours indicate the frequency of occurrence per parameter unit per unit height. The CFADs of cloud ice depict the frequency of cloud ice amounts within the horizontal domain between 300 to 500 km (e.g., Fig. 3b) and between hours 4-6 of the simulations.

Figure 5a shows the CFAD of cloud ice for case $PSFI_1RH$ (corresponding to Fig. 3b). Mixing ratios greater than 0.2 g kg^{-1} are seldom produced and most values are less than 0.1 g kg^{-1}. In contrast, the CFAD for case $PSFI_3RH$ (Fig. 5b) shows greater frequency of cloud ice mixing ratios exceeding 0.2 g kg^{-1} and significantly higher frequency of cloud ice above 10 km. For the same mixing ratio amount, the maximum frequency is found at a higher altitude in case $PSFI_3RH$ than in case $PSFI_1RH$. Using the modified HFO formulation ($PSFI_2$, Fig. 5c) yields results similar to the RH formulation (Fig. 5b). Apparently, the difference in magnitude between $PSFI_2$ and

$PSFI_3$ (Figs. 2b, c) produces only small changes to the cloud ice fields since the relative humidity tends to be near the ice saturation value.

Previously, it was mentioned that the ice particle masses calculated from the formula of RH were about an order of magnitude less than the values assumed in HFO. When the HFO particle masses are used instead of the RH values, the factor $\left[m_s^{(1-a_2)} - m_0^{(1-a_2)}\right]$ is about a factor of 7 larger so that the magnitude of PSFI is reduced by the same factor. Figure 5d shows that when the HFO particle masses are used in $PSFI_1$ (case $PSFI_1$HFO), the reduced values of PSFI contribute to increased ice mixing ratios. When the HFO particle masses are used in $PSFI_3$ (case $PSFI_3$HFO, Fig. 5e), the main differences from case $PSFI_3$RH are seen only between altitudes of 5-8 km, with little difference apparent above 8 km. The relative lack of sensitivity of $PSFI_3$ to the change in particle masses compared to $PSFI_1$ is due to the fact that, at altitudes above 8-10 km, the vapor mixing ratios are near or only slightly above the ice saturation value so that $PSFI_3$ is generally small. Since $PSFI_1$ is independent of supersaturation, a greater reduction of the conversion of ice to snow is achieved.

Another problem inherent in the dependence of PSFI on the assumed masses m_s and m_0 is that as the difference between m_s and m_0 becomes small, the conversion rate can become very rapid and lead to excessive depletion of cloud ice. If, on the other hand, the difference is large, then the conversion rate may become effectively negligible. Figure 6 shows the sensitivity of the different formulations of PSFI in Eqs. (4, 5, 8) to the size of the larger threshold particle size, i.e., the radius of particles with mass m_s, with m_s being calculated from the mass-diameter relationship of RH. The calculations assume 90% relative humidity with respect to water (120%

with respect to ice), air temperature of 243 K, and m_0 equal to the mass of a 40 micron radius particle. Significant sensitivity to the radius of the larger particle is seen between 50 and 100 microns.

Figure 5f (case $PSFI_3RH50$) shows that when m_s is reduced from that associated with a 100 micron radius particle to a 50 micron particle, the increase in $PSFI_3$ significantly reduces the cloud ice mixing ratios (compare to Fig. 5b). Somewhat less sensitivity to m_s is seen when the modified HFO formulation, $PSFI_2$, is used (Fig. 5g) because of the smaller exponent, e.g., $a_2 = 0.436$ for T<243 K compared to $a_2 = 0.5$ for $PSFI_3$. Reduced sensitivity is also found when the HFO values of m_s and m_0 are used (not shown) since these mass values are about an order of magnitude larger than in those from the RH mass-diameter formula. Hence, significant sensitivity of PSFI to m_s is found primarily in the RH formulation ($PSFI_3$) when the RH formula for ice mass versus diameter is used. Figure 6 suggests that using m_s equal to the mass of a 100 micron radius particle brings $PSFI_3$ into a range where it is less sensitive to small changes in m_s.

Krueger et al. (1995) suggested that the excessive conversion of ice to snow caused by $PSFI_1$ acts like a crude fallout of cloud ice since ice is assumed not to fall while snow does. This suggestion can be tested by including a small fall speed for cloud ice in the model. The formulation of PSFI assumes that the cloud ice particles are no larger than about 200 microns in diameter. Terminal velocities calculated by Heymsfield (1972) suggest maximum fall speeds of 20-30 cm s^{-1} for particles with lengths of 200 microns. Because of the uncertainty in fall velocities and their dependence on crystal habit, we simplify matters by using a constant fall velocity of 20 cm s^{-1} in the model. Figure 7 shows the snow and cloud ice fields for case

$PSFI_3RHVI$, which includes cloud ice fallout. The 20 cm s^{-1} fall speed has only a small effect on the snow and cloud ice distributions, the main effect being a lowering of the cloud top by about 1 km (cf. Figs. 4 and 7). Comparison of Fig. 7 to Fig. 3 also suggests that the excessive conversion of ice to snow by $PSFI_1$ is not equivalent to cloud ice fallout.

b. The saturation adjustment scheme

The saturation adjustment scheme in the GCE code is designed to account for condensation at warm temperatures ($T > 273$ K), deposition at temperatures less than 233 K, and a linear mix of the two at intermediate temperatures. Three problems exist with such a scheme. First, for 233 K $< T <$ 273 K, cloud water can be produced even when the relative humidity with respect to water is less than 100%. Second, for $T <$ 273 K, the scheme produces deposition in addition to the explicit calculation of deposition in the term PIDEP (see RH), if supersaturation with respect to ice is still present after the calculation of PIDEP and ice initiation, PINT (Appendix A). In particular, the effect is to produce more cloud ice at middle levels (243 K $< T <$ 273 K) than is parameterized by PIDEP. Finally, since the saturation adjustment scheme is computed prior to the depositional growth of snow and graupel, it reduces the depositional growth of the precipitation categories. This problem can be particularly troublesome in stratiform regions where significant growth of snow by deposition is known to occur (Rutledge and Houze 1987; Braun and Houze 1994; Houze 1997).

Figure 8 shows the snow and cloud ice distributions for case $PSFI_3RHNS$, which does not include the saturation adjustment with respect to ice. Snow mixing ratios (Fig. 8a) are comparable to the case with the saturation adjustment for ice ($PSFI_3RH$, Fig. 4a), but with slightly larger

snow mixing ratios in the trailing stratiform region. The cloud ice mixing ratios (Fig. 8b) are significantly reduced in the convective region and slightly reduced in the stratiform region. In particular, very little cloud ice is present below 8 km without the saturation adjustment for ice. These changes are quite evident in the CFAD for cloud ice (Fig. 5h), which shows mixing ratios rarely exceeding 0.1 g kg^{-1} above 8 km and 0.01 g kg^{-1} below. It is evident that a significant portion of the cloud ice is produced by the saturation adjustment scheme and not by the parameterized ice microphysical processes (PINT, PIDEP).

As mentioned above, one problem with the saturation adjustment scheme, when applied to cloud ice, is that it can produce cloud water when the relative humidity is less than 100% with respect to water. Figure 9 shows cloud water mixing ratios for cases $PSFI_3RH$ and $PSFI_3RHNS$. Figure 9a indicates that cloud water amounts for case $PSFI_3RH$ occasionally exceed 0.1 g kg^{-1} in regions that have relative humidities less than 98%, with these near saturated regions extending up to about 5.5 km. Figure 9b shows a qualitatively similar cloud water distribution in case $PSFI_3RHNS$, but in this case, cloud water is virtually always contained within regions having relative humidities exceeding 98%, with these near saturated regions extending up to about 8 km.

The relative humidities with respect to ice in cases $PSFI_3RH$ and $PSFI_3RHNS$ are quite different. For case $PSFI_3RH$ (Fig. 10a), the relative humidity field shows very uniform values near the ice saturation threshold within the anvil cloud above 9-10 km and relatively small supersaturations below 9 km. The relative humidity is very uniform at levels where T<233 K since the adjustment scheme brings the vapor mixing ratio to its saturation value, which is simply a function of temperature and has little small-scale variability within the upper portion of the cloud. Tendrils of cloud ice and high humidity hang down from the upper cloud canopy and

result from the saturation adjustment rather than from the explicit calculation of ice deposition in the term PIDEP. Since the supersaturations with respect to ice are small, the conversion rate $PSFI_3$ is also small. In contrast, in case $PSFI_3$RHNS (Fig. 10b), the relative humidity field shows more variability at upper levels and contains very high supersaturations between 6-8.5 km. There is no longer a constraint that the relative humidity be near the ice saturation value, but above 9 km, the relative humidity is still generally very close to this value. The tendrils of cloud ice are not apparent in this case since the ice deposition term PIDEP, being a strong function of temperature because of the Fletcher equation (Eq. A1), is unable to produce substantial amounts of ice at temperatures warmer than about 243 K. Furthermore, where the relative humidities with respect to ice are large, $PSFI_3$ rapidly converts the ice to snow.

The reduction in supersaturation by the saturation adjustment scheme (involving both cloud water and ice) before the calculation of snow depositional growth substantially reduces the potential growth of the snow field. Turning off the saturation adjustment for ice increases the relative humidity with respect to ice so that snow grows more by deposition, but it also reduces the amount of cloud ice so that snow grows less by conversion of ice to snow via PSFI and by accretion of cloud ice. This latter process, however, is highly dependent upon the collection efficiency of cloud ice by snow, the value of which is uncertain and probably overestimated in the model [see Eq. (23) and Fig. 4 of Lin et al. (1983)]. Consequently, turning off the saturation adjustment for ice may not necessarily lead to significant changes in snow production.

4. Conclusions

This note has described some potential problems associated with a parameterization of cloud ice processes that is used in many fine-scale cloud models, including the Goddard Cumulus

Ensemble (GCE) model. One problem is associated with the rate at which cloud ice is transferred to snow as a result of growth by vapor deposition, designated $PSFI_1$. The formulation generally used in the parameterization is independent of relative humidity, which causes ice to be converted to snow even when the air is subsaturated with respect to ice. Two alternative formulations are presented. The first alternative, designated $PSFI_2$, simply multiplies the original formula by an empirically derived relative-humidity dependent factor so that $PSFI_2$ diminishes as the relative humidity approaches the ice saturation value. The second alternative formulation, designated $PSFI_3$, is derived directly from the equation for depositional growth of cloud ice used in the model (PIDEP). This formulation causes $PSFI_3$ to diminish as the relative humidity approaches the ice saturation value, but also ensures physical consistency with the parameterization of depositional growth of cloud ice. The two alternative formulations produce relatively similar results. Their main impacts include an increase of cloud-top height and a substantial increase in the cloud ice mixing ratios, particularly at upper levels in the cloud.

A second issue of concern in the cloud ice parameterization is the use of a saturation adjustment technique for ice. While the technique is useful for generating cloud ice at temperatures warmer than about 243 K, it has the disadvantages in that it produces cloud water in slightly subsaturated air, forces cloudy air at cold temperatures (< 243 K) to have relative humidities at the ice saturation value, and prevents large supersaturations with respect to ice, which then limits the growth of snow by vapor deposition. Simulations in which the saturation adjustment was applied only to cloud water resulted in substantially reduced cloud ice amounts in the convective regions and nearly eliminated cloud ice at temperatures warmer than ~243 K. These results suggest that the saturation adjustment technique was responsible for generating a substantial portion of the cloud ice in convective cells and at temperatures where mixed-phase processes are important. A more realistic treatment of cloud ice processes should probably include cloud ice concentration as a prognostic variable in order to reduce the dependence of the ice scheme on the Fletcher equation for the number concentration of ice nuclei and should include improved formulations of the processes that produce cloud ice including ice multiplication mechanisms (e.g., Reisner et al. 1998).

Acknowledgments: The Goddard Cumulus Ensemble Model development and applications are supported by the NASA Headquarters Physical Climate Program and by the NASA TRMM project. The authors are grateful to Dr. R. Kakar (NASA/HQ) for his support of this research. Acknowledgment is also made to NASA Goddard Space Flight Center for computer time used in the research.

APPENDIX A

The number concentration of ice nuclei is specified according to Fletcher (1962) as

$$n_c = n_0 \exp\left[\beta(T_0 - T)\right], \tag{A1}$$

where T is temperature, T_0=273 K, and β and n_0 are often taken as 0.6 and 10^{-8} cm^{-3}, respectively[2]. One problem with the use of (A1) is that at very cold temperatures (T < 243 K), n_c attains unrealistically high values, which impacts the calculation of the initiation of new ice particles (PINT) and the depositional growth of existing ice particles (PIDEP). To avoid overestimates of n_c, two alternative solutions are 1) to limit (T_0-T) to some specified temperature deficit, say 31 K, or to limit the maximum concentration of ice to some prescribed value such as 1 cm^{-3}. The impact of these solutions is small when the saturation adjustment scheme is used but can be significant when the saturation adjustment scheme is not used (not shown).

The initiation of cloud ice, PINT, was formulated by Rutledge and Hobbs (1983) as

[2] We have changed β to 0.46 and n_c to 10^{-6} cm^{-3} in the simulations in this study because these values gave concentrations that were in better agreement with some observed values shown in Fig. 1 of Meyers et al. (1992). Tests with the model indicate only minor changes in the cloud ice mixing ratios produced by the changes in β and n_c.

$$\text{PINT} = \min\left[\frac{M_0 n_c}{\rho \Delta t}, \frac{q_v - q_{si}}{\Delta t}\right] \tag{A2}$$

where n_c is the prescribed number of ice particles, M_0 is the approximate mass of initiated ice particles, ρ is the density of air, and Δt is the model time step. This production term is assumed to produce n_c particles with mass M_0, unless it removes all of the existing supersaturation. At many grid points, cloud ice already exists when a supersaturation is produced. Rather than initiating n_c particles, PINT should initiate $n_c' = n_c - n_i$ particles ($n_i = \rho q_i / M_i$, M_i=average mass of existing ice particles), i.e., it should only initiate the number of particles needed to bring the concentration up to the prescribed number, n_c, possible at the ambient temperature. An alternative formulation of (A2) can be written as

$$\text{PINT} = \min\left[\frac{M_0 (n_c - n_i)}{\rho \Delta t}, \frac{q_v - q_{si}}{\Delta t}\right]. \tag{A3}$$

Equation (A3) is similar to the formulation used by Reisner et al. (1998). Model results indicate that replacing (A2) with (A3) in the microphysical scheme produces only relatively small changes in the cloud ice field.

REFERENCES

Braun, S. A., and R. A. Houze, Jr., 1994: The transition zone and secondary maximum of radar reflectivity behind a midlatitude squall line: Results retrieved from Doppler radar data. *J. Atmos. Sci.*, **51**, 2733-2755.

Cunning, J. B., 1986: The Oklahoma-Kansas Preliminary Regional Experiment for STORM-Central. *Bull. Amer. Meteor. Soc.*, **67**, 1478-1486.

Dudhia, J, 1989: Numerical study of convection observed during the winter monsoon experiments using a mesoscale two-dimensional model. *J. Atmos. Sci.*, **46**, 3077-3107.

Fletcher, N. H., 1962: *The Physics of Rain Clouds*. Cambridge University Press, 390 pp.

Heymsfield, A., 1972: Ice crystal terminal velocities. *J. Atmos. Sci.*, **29**, 1348-1357.

Hindman, E. E., and D. B. Johnson, 1972: Numerical simulation of ice particle growth in a cloud of supercooled water droplets. *J. Atmos. Sci.*, **29**, 1313-1321.

Houze, R. A., Jr., 1997: Stratiform precipitation in regions of convection: A meteorological paradox? *Bull. Amer. Meteor. Soc.*, **78**, 2179-2196.

Hsie, E. Y., R. D. Farley, and H. D. Orville, 1980: Numerical simulation of ice-phase convective cloud seeding. *J. Appl. Meteor.*, **19**, 950-977.

Johnson, R. H., and P. J. Hamilton, 1988: The relationship of surface pressure features to the precipitation and airflow structure of an intense midlatitude squall line. *Mon. Wea. Rev.*, **116**, 1444-1472.

Klemp, J. B., and R. Wilhelmson, 1978: The simulation of three-dimensional convective storm dynamics. *J. Atmos. Sci.*, **35**, 1070-1096.

Koenig, L. R., 1971: numerical modeling of ice deposition. *J. Atmos Sci.*, **28**, 226-237.

Krueger, S. K., Q. Fu, K. N. Liou, and H.-N. S. Chen, 1995: Improvements of an ice-phase microphysics parameterization for use in numerical simulations of tropical convection. *J. Appl. Meteor.*, **34**, 281-287.

Lin, Y.-L., R. D. Farley, and H. D. Orville, 1983: Bulk parameterization of the snow field in a cloud model. *J. Climate Appl. Meteor.*, **22**, 1065-1092.

Liu, Y., D.-L. Zhang, and M. K. Yau, 1997: A multiscale numerical study of Hurricane Andrew (1992). Part I: Explicit simulation and verification. *Mon. Wea. Rev.*, **125**, 3073-3093.

Meyers, M. P., P. J. DeMott, and W. R. Cotton, 1992: New primary ice-nucleation parameterizations in an explicit cloud model. *J. Appl. Meteor.*, **31**, 708-721.

Reisner, J., R. M. Rasmussen, and R. T. Bruintjes, 1998: Explicit forecasting of supercooled liquid water in winter storms using the MM5 mesoscale model. *Quart. J. Roy. Meteor. Soc.*, **125**, 1071-1108.

Rutledge, S A., and P. V. Hobbs, 1983: The mesoscale and microscale structure and organization of clouds and precipitation in midlatitude cyclones. VIII: A model for the "seeder-feeder" process in warm frontal rainbands. *J. Atmos. Sci.*, **40**, 1185-1206.

————, and ————, 1984: The mesoscale and microscale structure and organization of clouds and precipitation in midlatitude cyclones. XII: A diagnostic modeling study of precipitation development in narrow cold-frontal rainbands. *J. Atmos. Sci.*, **41**, 2949-2972.

————, and R. A. Houze, Jr., 1987: A diagnostic modeling study of the stratiform region associated with a tropical squall line. *J. Atmos. Sci.*, **43**, 1356-1377.

————, ————, M. I. Biggerstaff, and T. Matejka, 1988: The Oklahoma-Kansas mesoscale convective system of 10-11 June 1985: Precipitation structure and single-Doppler radar analysis. *Mon. Wea. Rev.*, **116**, 1409-1430.

Smolarkiewicz, P. K., and W. W. Grabowski, 1990: The multi-dimensional positive advection transport algorithm: Nonoscillatory option. *J. Comput. Phys.*, **86**, 355-375.

Tao, W.-K., and S.-T. Soong, 1986: A study of the response of deep tropical clouds to mesoscale processes: Three-dimensional numerical experiments. *J. Atmos. Sci.*, **43**, 2653-2676.

————, and J. Simpson, 1993: The Goddard Cumulus Ensemble Model. Part I: Model description. *Terr., Atmos. Oceanic Sci.*, **4**, 35-72.

————, ————, and M McCumber, 1989: An ice-water saturation adjustment. *Mon. Wea. Rev.*, **117**, 231-235.

————, ————, C.-H. Sui, B. S. Ferrier, S. Lang, J. Scala, M.-D. Chou, and K. Pickering, 1993: Heating, moisture and water budgets of tropical and midlatitude squall lines: Comparisons and sensitivity to longwave radiation. *J. Atmos. Sci.*, **50**, 673-690.

————, S. Lang, J. Simpson, C.-H. Sui, B. S. Ferrier, and M.-D. Chou, 1996: Mechanisms of cloud-radiation interaction in the tropics and midlatitudes. *J. Atmos. Sci.*, **53**, 2624-2651.

Yuter, S. E., and R. A. Houze, Jr., 1995: Three-dimensional kinematic and microphysical evolution of Florida cumulonimbus. Part II: Frequency distributions of vertical velocity, reflectivity, and differential reflectivity. *Mon. Wea. Rev.*, **123**, 1941-1963.

Table 1. Summary of the numerical simulations. The column labeled "ice mass" indicates whether the HFO or RH values are used for the initial and final sizes of ice crystals, m_0 and m_s, the values of which are provided in the last two columns. Case $PSFI_3RHVI$ differs from $PSFI_3RH$ in that it includes a fall velocity for cloud ice. Case $PSFI_3RHNS$ differs from $PSFI_3RH$ in that it does not use the saturation adjustment for cloud ice.

Name	*PSFI Formulation*	*Ice Mass*	m_0 (g)	m_s (g)
$PSFI_1RH$	$PSFI_1$	RH	2.41×10^{-8}	1.51×10^{-7}
$PSFI_2RH$	$PSFI_2$	RH	2.41×10^{-8}	1.51×10^{-7}
$PSFI_3RH$	$PSFI_3$	RH	2.41×10^{-8}	1.51×10^{-7}
$PSFI_1HFO$	$PSFI_1$	HFO	2.46×10^{-7}	3.84×10^{-6}
$PSFI_2HFO$	$PSFI_2$	HFO	2.46×10^{-7}	3.84×10^{-6}
$PSFI_3HFO$	$PSFI_3$	HFO	2.46×10^{-7}	3.84×10^{-6}
$PSFI_2RH50$	$PSFI_2$	RH	2.41×10^{-8}	3.76×10^{-8}
$PSFI_3RH50$	$PSFI_3$	RH	2.41×10^{-8}	3.76×10^{-8}
$PSFI_3RHVI$	$PSFI_3$	RH	2.41×10^{-8}	1.51×10^{-7}
$PSFI_3RHNS$	$PSFI_3$	RH	2.41×10^{-8}	1.51×10^{-7}

FIGURE CAPTIONS

Figure 1. Curves of a_1 as a function of temperature. The solid line shows the values from Koenig (1971) while the dashed line shows the values for the new formulation of $PSFI_3$. For the latter values, a relative humidity of 100% has been assumed in order to be consistent with Koenig.

Figure 2. Magnitude (in units of 10^{-7} g g^{-1} s^{-1}) of the various formulations of PSFI: a) the original HFO formulation (Eq. 4), b) the modified HFO formulation (Eq. 5), and c) the RH formulation (Eq. 8). Temperature is shown along the vertical axis of the plots as a proxy for height. For these calculations, the temperature was assumed to vary in the vertical according to the 2330 UTC Pratt, Kansas, sounding. Solid lines in (a-c) indicate conversion rates, thick dashed lines supersaturation with respect to ice. (d) Difference between $PSFI_1$ and $PSFI_3$, with positive (negative) values indicated by solid (dashed) lines.

Figure 3. Vertical cross sections of time-averaged (a) snow mixing ratio and (b) cloud ice mixing ratio for case $PSFI_1RH$. Cross sections were obtained by averaging fields from hours 5-6 using output at 10-min intervals. The contour intervals are 0.1 g kg^{-1} starting at 0.01 g kg^{-1} for snow and 0.025 g kg^{-1} starting at 10^{-3} g kg^{-1} for cloud ice.

Figure 4. Same as in Fig. 3, but for case $PSFI_3RH$.

Figure 5. Contoured Frequency by Altitude Diagrams (CFADs) for cloud ice mixing ratio. Contours indicate the frequency km^{-1} $(g\ kg^{-1})^{-1}$. Contours are drawn at values of 0.5, 1, 2, 4, 8, 12, 20, 36, 48, 60, and 72. The 4 km^{-1} $(g\ kg^{-1})^{-1}$ contour is highlighted by the dashed line.

Figure 6. Sensitivity of PSFI to the threshold radius of snow corresponding to the mass m_s in Eqs. (4, 5, and 8).

Figure 7. Same as in Fig. 4 (case $PSFI_3RH$), but for case $PSFI_3RHVI$, which includes a fall velocity for cloud ice.

Figure 8. Same as in Fig. 4 (case $PSFI_3RH$), but for case $PSFI_3RHNS$, which does not use the saturation adjustment for cloud ice.

Figure 9. Vertical cross sections at t=6 h of cloud water (contours) and relative humidity with respect to water (shading) for cases (a) $PSFI_3RH$ (with the saturation adjustment for ice) and (b) $PSFI_3RHNS$ (without the saturation adjustment for ice). Shading indicates regions with relative humidity exceeding 98%. Contours for cloud water are drawn at values of 0.01, 0.1, 0.5, 1, 2, and 3 $g\ kg^{-1}$.

Figure 10. Vertical cross sections at t=6 h of cloud ice (contours) and relative humidity with respect to ice (shading) for cases (a) $PSFI_3RH$ (with the saturation adjustment for ice) and (b) $PSFI_3RHNS$ (without the saturation adjustment for ice). Shading indicates regions with relative

humidity exceeding 100% (light shade), 110% (dark shade), and 120% (white). Contours for cloud ice are drawn at values of 0.01, 0.05, 0.1, 0.15, 0.2, and 0.3 g kg^{-1}.

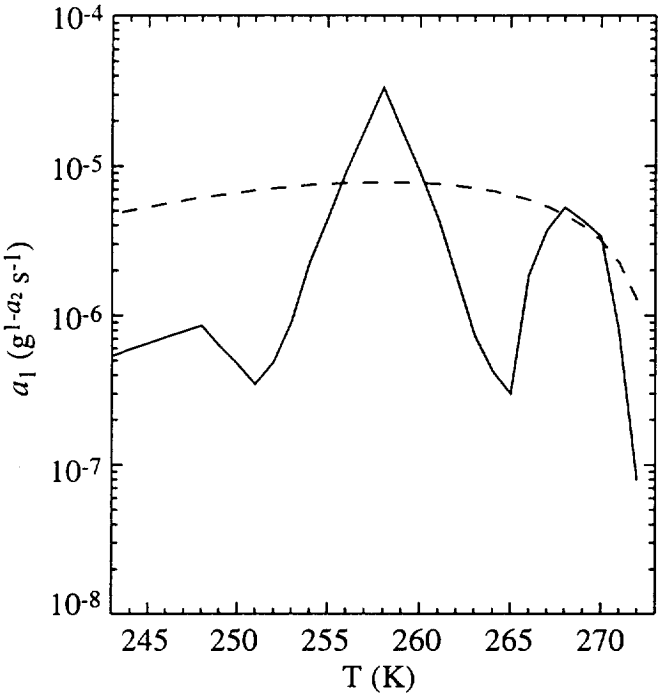

Figure 1. Curves of a_1 as a function of temperature. The solid line shows the values from Koenig (1971) while the dashed line shows the values for the new formulation of $PSFI_3$. For the latter values, a relative humidity of 100% has been assumed in order to be consistent with Koenig.

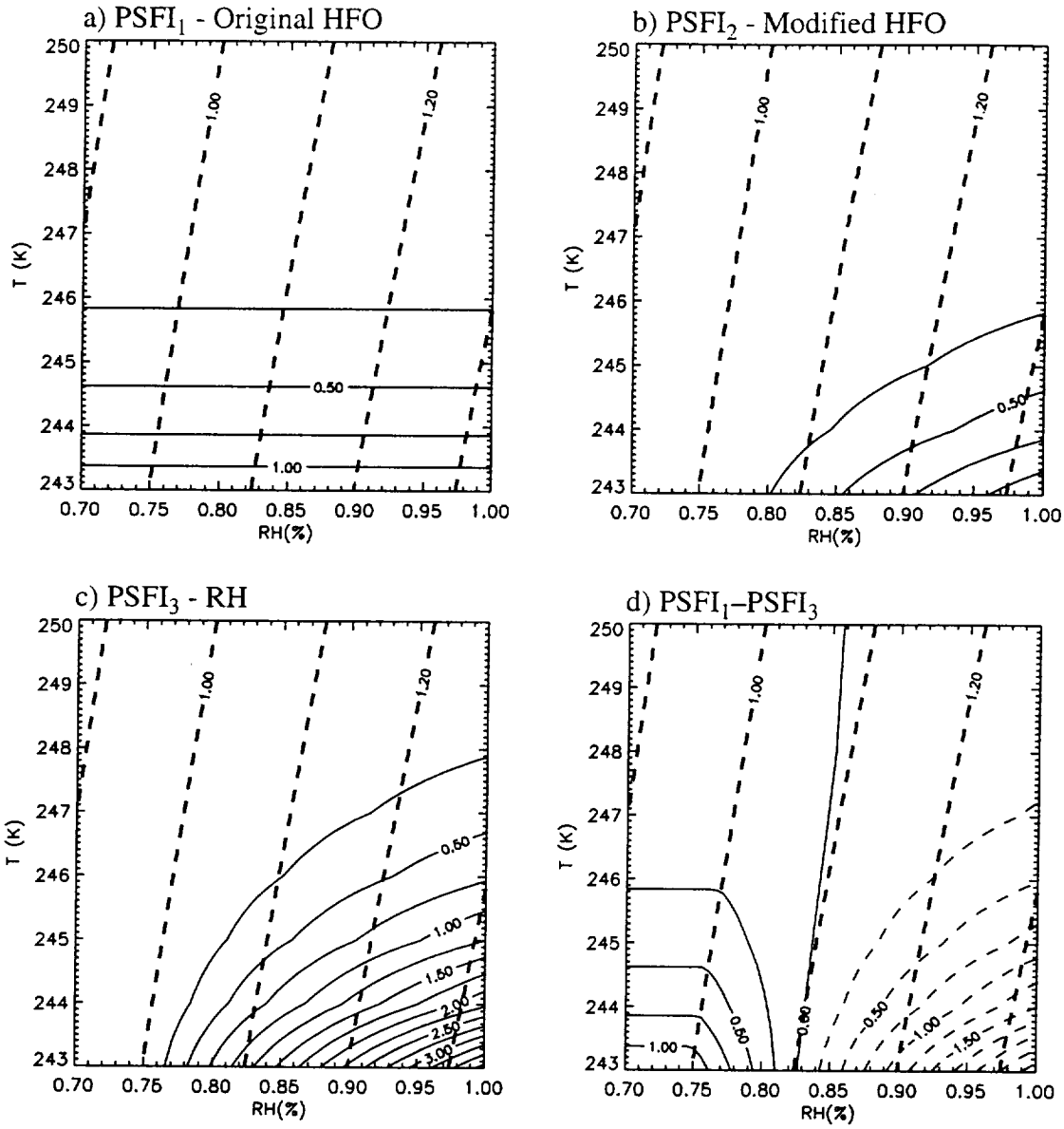

Figure 2. Magnitude (in units of 10^{-7} g g^{-1} s^{-1}) of the various formulations of PSFI: (a) the original HFO formulation (Eq. 4), (b) the modified HFO formulation (Eq. 5), and (c) the RH formulation (Eq. 8). Temperature is shown along the vertical axis of the plots as a proxy for height. For these calculations, the temperature was assumed to vary in the vertical according to the 2330 UTC Pratt, Kansas, sounding. Solid lines in (a-c) indicate conversion rates, thick dashed lines supersaturation with respect to ice (q_v/q_{si}). (d) Difference between $PSFI_1$ and $PSFI_3$, with positive (negative) values indicated by solid (dashed) lines.

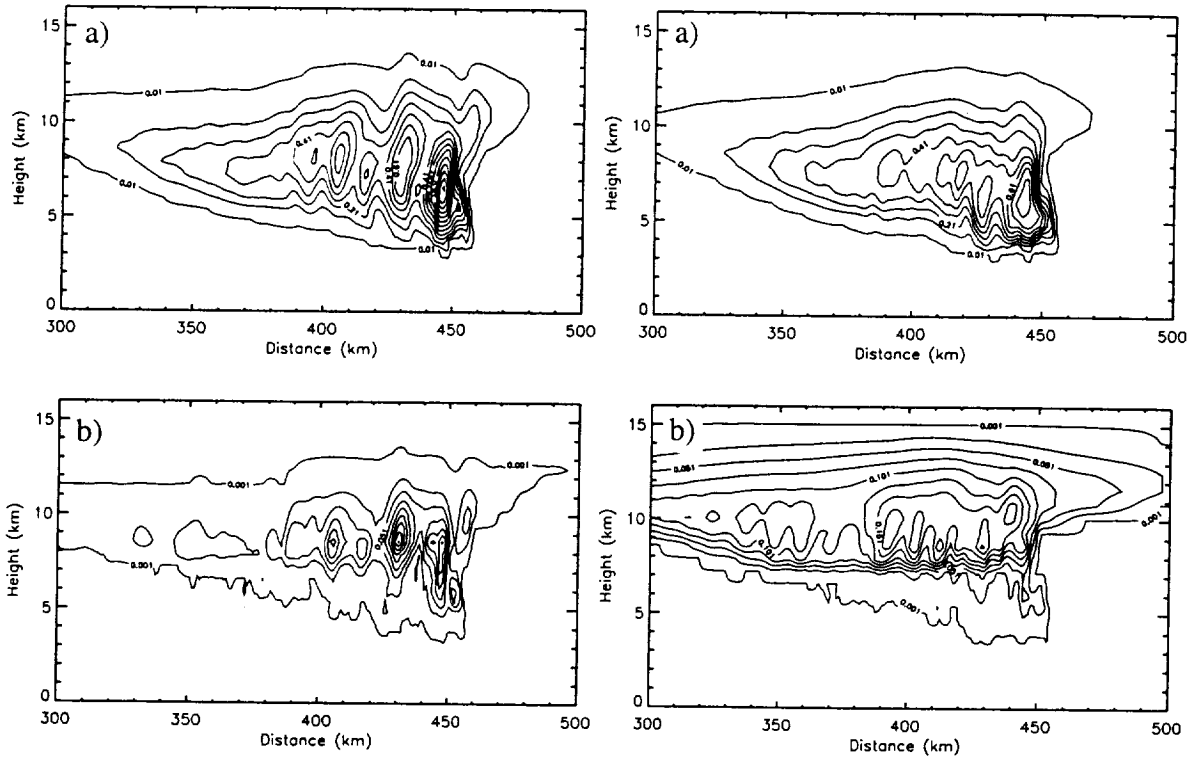

Figure 3. Vertical cross sections of time-averaged (a) snow mixing ratio and (b) cloud ice mixing ratio for case $PSFI_1RH$. Cross sections were obtained by averaging fields from hours 5-6 using output at 10-min intervals. The contour intervals are 0.1 g kg^{-1} starting at 0.01 g kg^{-1} for snow and 0.025 g kg^{-1} starting at 0.001 g kg^{-1} for cloud ice.

Figure 4. Same as in Fig. 3, but for case $PSFI_3RH$.

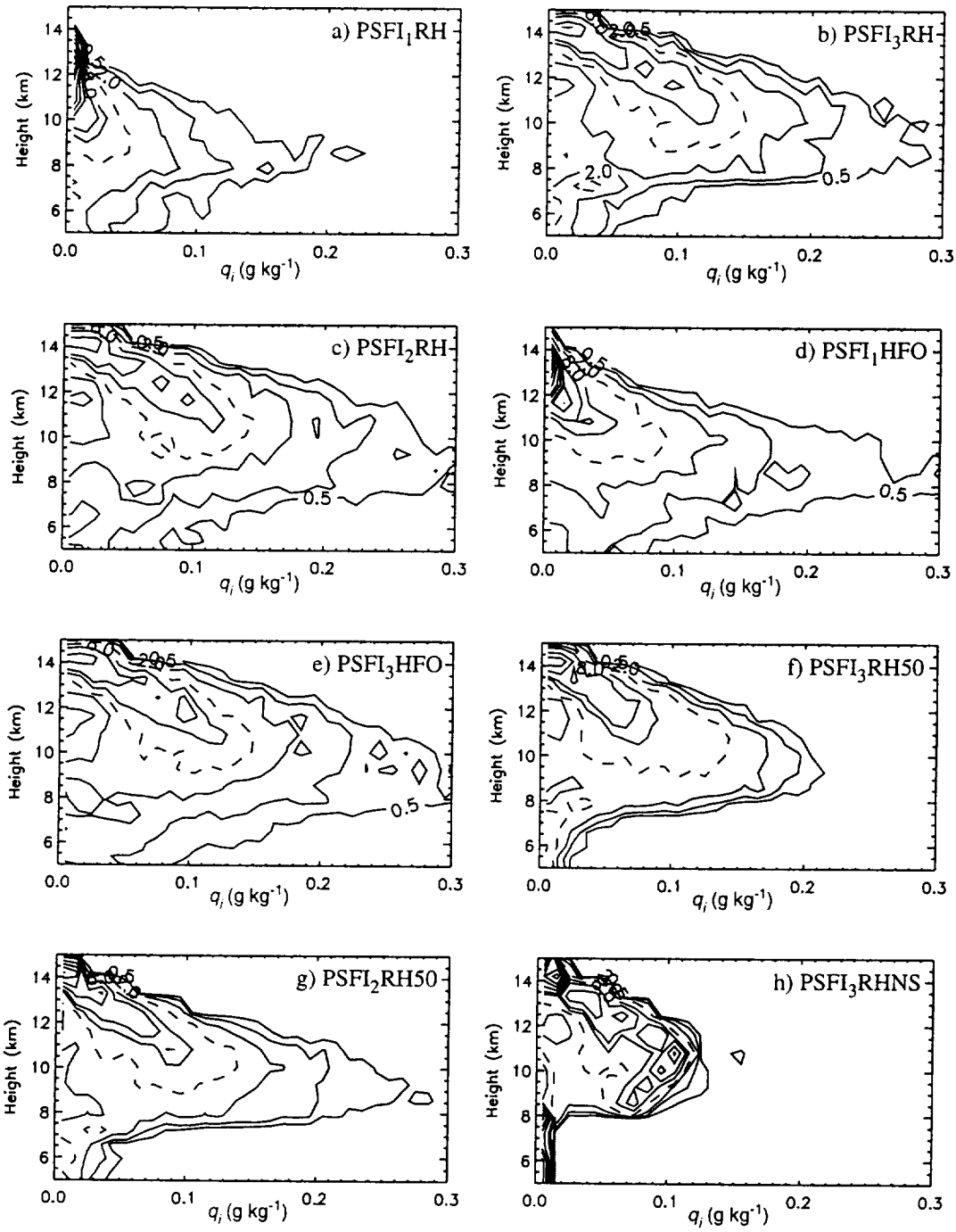

Figure 5. Contoured Frequency by Altitude Diagrams (CFADs) for cloud ice mixing ratio. Contours indicate the frequency km^{-1} $(g\ kg^{-1})^{-1}$. Contours are drawn at values of 0.5, 1, 2, 4, 8, 12, 20, 36, 48, 60, and 72. The 4 km^{-1} $(g\ kg^{-1})^{-1}$ contour is highlighted by the dashed line.

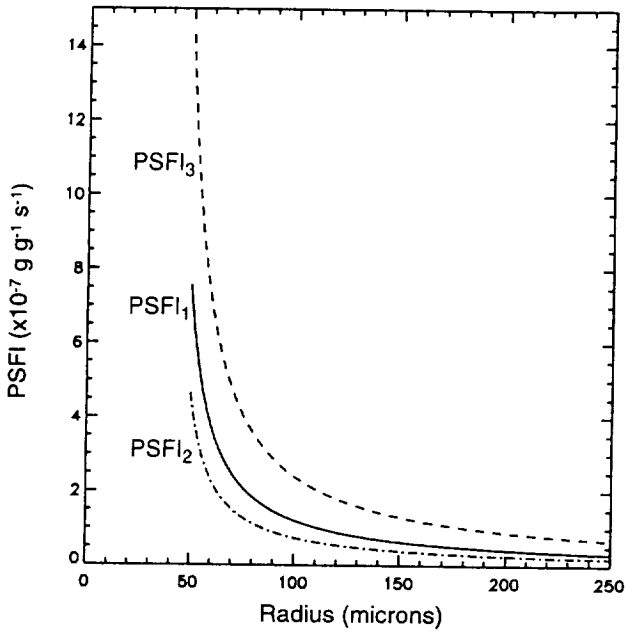

Figure 6. Sensitivity of PSFI to the threshold radius of snow corresponding to the mass m_s in Eqs. (4,5, and 8).

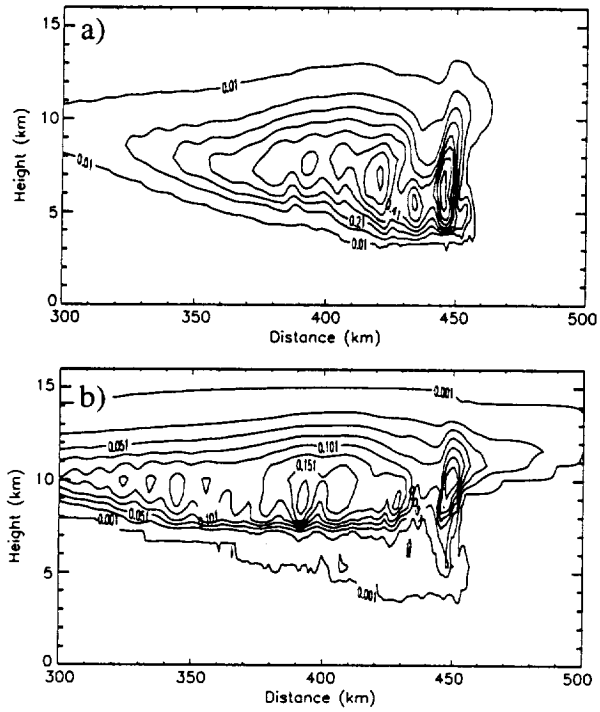

Figure 7. Same as in Fig. 4 (case $PSFI_3RH$), but for case $PSFI_3RHVI$, which includes a fall velocity for cloud ice.

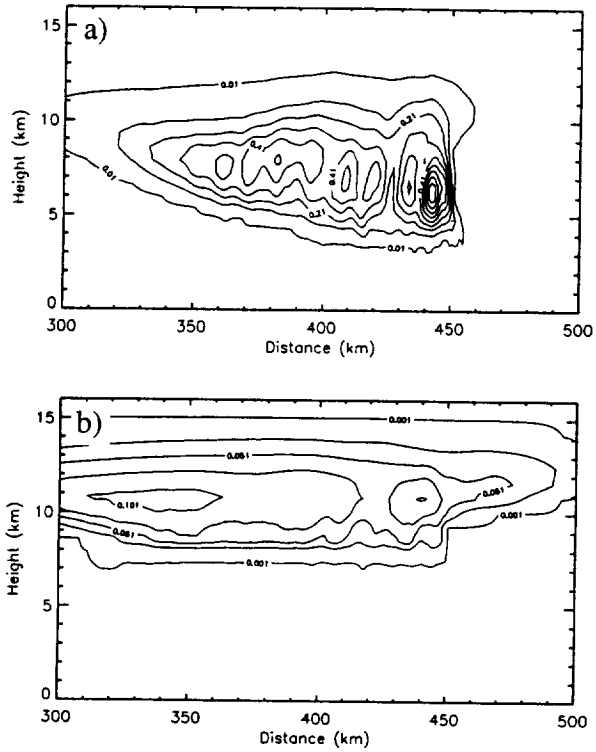

Figure 8. Same as Fig. 4 (case $PSFI_3RH$), but for case $PSFI_3RHNS$, which does not use the saturation adjustment for cloud ice.

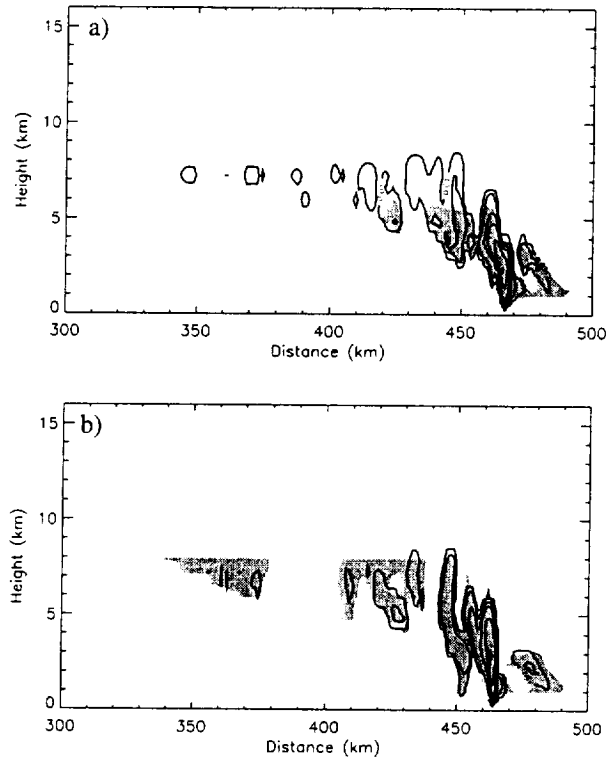

Figure 9. Vertical cross sections at t=6 h of cloud water (contours) and relative humidity with respect to water (shading) for cases (a) PSFI$_3$RH (with the saturation adjustment for ice) and (b) PSFI$_3$RHNS (without the saturation adjustment for ice). Shading indicates regions with relative humidity exceeding 98%. Contours for cloud water are drawn at values of 0.01, 0.1, 0.5, 1, 2, and 3 g kg^{-1}.

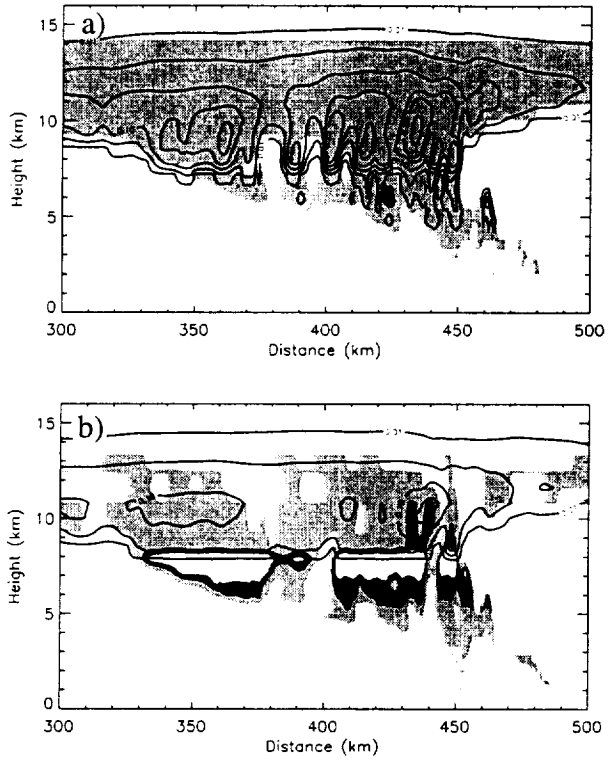

Figure 10. Vertical cross sections at t=6 h of cloud ice (contours) and relative humidity with respect to ice (shading) for cases (a) $PSFI_3RH$ (with the saturation adjustment for ice) and (b) $PSFI_3RHNS$ (without the saturation adjustment for ice). Shading indicates regions with relative humidity exceeding 100% (light shade), 110% (dark shade), and 120% (white). Contours for cloud ice are drawn at values of 0.01, 0.05, 0.1, 0.15, 0.2, and 0.3 g kg^{-1}.